



Construction and identification of highly active single-atom Fe₁-NC catalytic site for electrocatalytic nitrate reduction

Lingyue Liu ^{a,1}, Ting Xiao ^{b,1}, Heyun Fu ^a, Zhongjun Chen ^c, Xiaolei Qu ^a, Shourong Zheng ^{a,*}

^a State Key Laboratory of Pollution Control and Resource Reuse, School of the Environment, Nanjing University, Nanjing 210046, China

^b The Institute for Advanced Studies, Wuhan University, Wuhan 430072, China

^c Institute of High Energy Physics, Chinese Academy of Sciences, Beijing 100049, China



ARTICLE INFO

Keywords:
Fe-N-C single atom catalysts
Nitrate reduction reaction
Coordination structures
Geometry structures
Operando ATR-SEIRAS

ABSTRACT

Atomically dispersed metal-N-C sites are highly active and selective for nitrate reduction reaction (NO₃RR), while identifying their coordination and geometry structures remains significantly challenging. In this study, thermal-modulated single-atom Fe-based catalysts were fabricated and applied in NO₃RR. The coordination and geometry structures of metal active-site in the Fe₁/NC-X (X is the pyrolysis temperature) catalysts were elaborately dissected. The results disclose that Fe₁/NC-900 with trigonal pyramidal Fe-N₃ coordination exhibits the highest NO₃RR performance with an ammonia yield rate (YR) of 18.8 mg_{NH3} h⁻¹ mg_{cat}⁻¹ at -0.9 V, and a Faradaic efficiency (FE) of 86% at -0.7 V vs RHE. Electrochemical *operando* attenuated total reflection surface-enhanced infrared absorptive spectroscopy (ATR-SEIRAS) and density functional theory (DFT) calculation demonstrate that the Fe-N₃ coordination in Fe₁/NC-900 are responsible for the much higher catalytic activity in NO₃RR due to their lone pair electrons, stronger charge transfer, and lower energy barrier of the rate-determining step.

1. Introduction

As an indispensable foundational compound, ammonia (NH₃) is commonly produced by the industrial-scale Haber-Bosch process, which is energy-consuming [1]. Electrochemical N₂ reduction reaction (NRR) has attracted increasing attention, which enables direct NH₃ production from the coupling of N₂ and H₂O under mild conditions [2,3]. While, the challenge lies in the activation of nonpolar N≡N bond with high cleavage energy (941 kJ/mol) and low N₂ solubility in electrolytes, leading to the very low NH₃ selectivity and yield rate (YR) [4]. In contrast to NRR, electrocatalytic nitrate reduction reaction (NO₃RR) does not require the dissociation of high-energy bonds, thus achieving faster rate for NH₃ production [5,6]. It should be mentioned that the accelerating exploitation and utilization of nitrogen-containing compounds has brought global nitrate contamination in water environment. Thus, converting nitrate into valuable and recyclable NH₃ is alluring [7–9]. However, NO₃RR is accomplished by multiple electron/protons transfer along with strong competition from hydrogen evolution reaction (HER), which deteriorates NH₃ YR and Faradaic efficiency (FE) [10, 11]. Thus, efficient NO₃RR catalysts are urgently required for selective and stable NH₃ production.

Single-atom catalysts (SACs) usually possesses high activity and selectivity toward specific products and thus have been widely applied in various reactions, such as CO₂ reduction reaction (CO₂RR) [12–14], HER [15,16], and NO₃RR [17,18]. For NO₃RR, atomically dispersed Fe-nitrogen modified carbon nanomaterials (Fe₁/NC) have been regarded as efficient catalysts for NH₃ production [19–21]. Particularly, Fe₁/NC lacks adjacent metal sites, preventing N-N coupling and promoting NH₃ selectivity in NO₃RR [22]. Previous studies have shown that rational regulation of the coordination environment of SACs can change the electronic and geometric structure of the central metal atom, thus changing the absorption of reactants on the metal atom and affecting the catalytic performance [23,24]. Variation of the pyrolysis temperature is an effective way to regulating the coordination environment of Fe SACs, while clear identification of the active sites of Fe₁/NC, such as Fe-N_x (x = 1–4), Fe-Cy (y = 1–4), is very difficult [25,26]. Currently, x-ray absorption fine structure (XAFS) technology is the most powerful tool to tackle this challenge [27–29]. However, simple utilization of XAFS to determine coordination number is not accurate enough, generally providing little information on the active site geometry. Hence, powerful characterization tools and comprehensive analytical methods are indispensable to explore the metal-N-C structure.

* Corresponding author.

E-mail address: srzheng@nju.edu.cn (S. Zheng).

¹ These authors contributed equally to this work.

Herein, we constructed a series of single atom Fe/NC catalysts by pyrolysis at 800–1000 °C (denoted as $\text{Fe}_1/\text{NC-X}$, X is the pyrolysis temperature). Detailed XAFS and soft XAS investigation disclose that $\text{Fe}_1/\text{NC-800}$, $\text{Fe}_1/\text{NC-900}$, and $\text{Fe}_1/\text{NC-1000}$ have dominantly active sites with $\text{Fe}-\text{N}_4-\text{OH}$ (the square-based pyramidal with a OH at the apex), $\text{Fe}-\text{N}_3$ (trigonal pyramidal) and $\text{Fe}-\text{N}_4$ (slightly broken square-planar) configurations, respectively. Among them, $\text{Fe}_1/\text{NC-900}$ exhibits superior $\text{NO}_3^{\cdot}\text{RR}$ performances with a FE of 86.7% and a YR of 18.8 mg NH_3 h $^{-1}$ mg $^{-1}$ cat^{-1} . *Operando* attenuated total reflection surface-enhanced infrared absorptive spectroscopy (ATR-SEIRAS) observed various N-containing intermediates in $\text{NO}_3^{\cdot}\text{RR}$. Combined with density functional theory (DFT), the reaction mechanism of $\text{NO}_3^{\cdot}\text{RR}$ is elucidated.

2. Experimental

2.1. Preparation of catalysts

To prepare Fe SAC with different coordination and geometry structures, a conventional pyrolysis strategy was applied (Fig. 1). First, 8 g melamine ($\text{C}_3\text{H}_6\text{N}_6$), 1.5 g L-alanine ($\text{C}_3\text{H}_7\text{NO}_2$) and 4 mg Iron chloride hexahydrate ($\text{FeCl}_3 \bullet 6 \text{ H}_2\text{O}$) were mixed and grounded using zirconia grinding media until it became homogeneous. Then, 10 mL mixed solution of ethanol and hydrochloric acid (volume ratio 4:1) was added. The slurry continued to be grinded until the ethanol evaporated. The mixture was dried in an oven at 80 °C and ball milled again for 10 min. Subsequently, the fine powder mixture was undergone a two-stage pyrolysis and carbonization process at Ar atmosphere. These processes were performed (i) heating from room temperature to 550 °C and held at 550 °C for 2 h, (ii) heating from 550 °C to 900 °C and then held at that temperature for 1.5 h. During heating treatment, the temperature was ramped from room temperature to 550 °C at a rate of 2 °C/min, then further ramped to the target temperature at a rate of 2 °C/min and cooled down at same rate in laboratory conditions. Hereafter the sample was collected and denoted as $\text{Fe}_1/\text{NC-900}$. Identical method was carried out for the target temperatures of 800 °C and 1000 °C, respectively, denoted as $\text{Fe}_1/\text{NC-800}$ and $\text{Fe}_1/\text{NC-1000}$. The coordination and geometric structures of the metal active sites in $\text{Fe}_1/\text{NC-800}$, $\text{Fe}_1/\text{NC-900}$ and $\text{Fe}_1/\text{NC-1000}$ catalysts are $\text{Fe}-\text{N}_4-\text{OH}$ with a square-based pyramidal with a OH at the apex, $\text{Fe}-\text{N}_3$ with a trigonal pyramidal and $\text{Fe}-\text{N}_4$ with a slightly broken square-planar, respectively, which is derived from detailed analysis from the XAS technique (see more discussion in Section 3.3).

2.2. Characterization

Powder x-ray diffraction (XRD) data was obtained using a Bruker D8 diffractometer with $\text{Cu K}\alpha$ ($\lambda = 1.5406 \text{ \AA}$) radiation. Diffraction patterns were recorded between 10° and 80° with a step size of 0.05° /s. Raman spectroscopy was measured with the Raman microscope (JY-HR800, λ excited=532 nm). Field-emission scanning electron microscopy (FESEM) images were recorded via a ZEISS Merlin Compact SEM

equipped with an EDX spectrometer (INCA PentaFETx3 Oxford EDX). The tapping mode was adopted in transmission electron microscopy (TEM, JEOL JEM-210). Sub-ångström-resolution high-angle annular dark-field scanning transmission electron microscopy (HAADF-STEM) characterization was conducted on a JEOL JEMARM200F STEM/TEM with a guaranteed resolution of 0.08 nm. X-ray photoelectron spectroscopy (XPS) measurements were performed a VG twin-crystal spectrometer with a double-focusing hemispherical electron analyzer (Thermo Scientific, ESCALAB250Xi) in a standard ultrahigh vacuum chamber. The samples were probed with a photon energy of $h\nu = 1486.58 \text{ eV}$ produced by a monochromatized $\text{Al K}\alpha$ source. The total energy resolution was 0.45 eV, and the step size for all measured spectra was 0.02 eV. Soft X-ray absorption spectroscopy (soft-XAS) and Fe K -edge XAS measurements were performed at the 4B9B and 4B9A beamline of Beijing Synchrotron Radiation Facility (BSRF) in Beijing, respectively. The analysis of XAS is represented detailly in Supporting information.

2.3. Electrochemical measurements

The electrochemical measurements were carried out in a customized H-type glass cell separated by Nafion 117 membrane (Fuel Cell Store) at room temperature. A CHI 660D electrochemical workstation (Chenhua, Shanghai) was used to record the electrochemical response. The $\text{Fe}_1/\text{NC-X}$ sample on carbon paper, saturated Ag/AgCl electrode and platinum foil was used as the working electrode, reference electrode and counter electrode, respectively. All potentials in this study were measured against the SCE and converted to the RHE reference scale by $E (\text{V vs. RHE}) = E (\text{V vs. SCE}) + 0.0591 \text{ pH} + 0.241$. The working electrode was prepared as follows: 5 mg of $\text{Fe}_1/\text{NC-X}$ catalyst powder, 980 μl of ethanol-deionized water mixed solution (the volume ration of ethanol and deionized water is 1:1), and 20 μl Nafion solution (Sigma Aldrich, 5 wt%) were mixed and sonicated for at least 3 h to form a homogeneous ink. Then, all the catalyst ink was drop-casted onto carbon paper with 1 cm × 5 cm. The surface area of carbon paper was $1 \text{ mg} \bullet \text{cm}^{-2}$ as the working electrode. For electrocatalytic NO_3^{\cdot} reduction, a solution with 0.1 M K_2SO_4 and 0.5 M KNO_3 was used as the electrolyte unless otherwise specified and was evenly distributed to the cathode and anode compartment. The electrolyte volume in the two parts of H-cell was 50 mL and was purged with high-purity Ar for 10 min before the measurement. The LSV was performed at a rate of 5 mV s^{-1} . The potentiostatic tests was conducted at constant potentials for 1 h at a stirring rate of 500 r.p.m. High-purity Ar was continuously fed into the cathodic compartment during the experiments. For consecutive recycling test, the potentiostatic tests were performed at -0.7 V for 1 h at a stirring rate of 500 r.p.m. After electrolysis, the electrolyte was analyzed by UV-vis spectrophotometry as mentioned below. Then, the potentiostatic tests were carried out at the same conditions using the fresh electrolyte for the next cycle.

The YR of NH_3 can be calculated using the following equation:

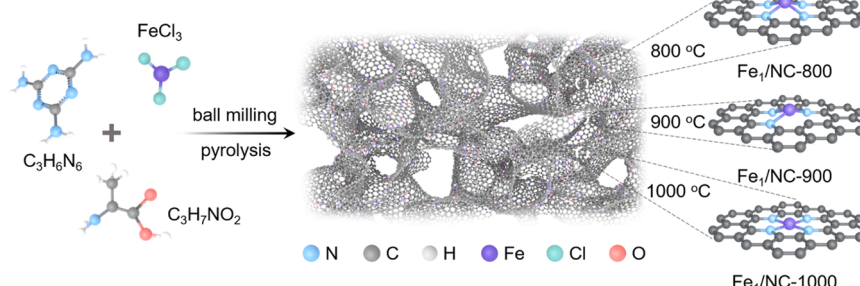


Fig. 1. Schematic of the synthesis process for $\text{Fe}_1/\text{NC-X}$.

$$\text{NH}_3 \text{ yield rate} = \frac{(C_{\text{NH}_3} \times V)}{(t \times A)} \times 10^{-3} \quad (1)$$

The FE of NH_3 is the percentage of the charge consumed for NH_3 generation in the total charge passed through the electrode according to the equation below:

$$\text{FE}_{(\text{NH}_3)} = \frac{(8 \times F \times C_{\text{NH}_3} \times V \times 10^{-6})}{(17 \times Q)} \times 100\% \quad (2)$$

where C_{NH_3} is the measured NH_3 concentration ($\mu\text{g mL}^{-1}$); V is the volume of the electrolyte (50 mL); t is the electrolysis time (1 h); A is the geometric area of the electrode (1 cm^2); F is the faraday constant ($96,485 \text{ C mol}^{-1}$); Q (C) is the total charge passed through the electrode, which is the integral of $I-t$ curve. The yield rate, the faradaic efficiency, and corresponding error bars were obtained from three individual samples under the same testing conditions.

2.4. Operando surface-enhanced infrared absorptive spectroscopy (SEIRAS)

Attenuated total reflection-SEIRAS was performed (Bruker Invenio S FTIR spectrometer) to get insight into the nitrate reduction mechanism. A custom-made electrochemical cell setup with a Si face-angled crystal was used on a VeeMax III variable angle accessory. To enhance the metal wettability of the Si crystal, it was sputter-coated with an IR transparent indium tin oxide (ITO) to form a 53 nm thick ITO layer using a film thickness monitored sputtering (EMS Quorum 150TS plus). Au was sputtered on top of this ITO layer with a thickness of 13 nm. The spectra were acquired at -0.1 V to -1.0 V vs. RHE. Each spectrum was

acquired with a resolution of 2 cm^{-1} using a liquid N_2 cooled mid-band mercury cadmium telluride (MCT) detector and averaged over 128 scans.

2.5. Density functional theory (DFT) calculations

Our computational simulations were performed using Vienna ab-initio simulation package (VASP-sol) with the projector augmented wave pseudo-potentials (PAW) to describe the interaction between atomic cores and valence electrons with density functional theory (DFT). The Perdew–Burke–Ernzerhof (PBE) functional within the generalized gradient approximation (GGA) were used to implement DFT calculations [30]. The reasonable vacuum layers were set around 15 \AA in the z-direction for avoiding interaction between planes. A cutoff energy of 500 eV was provided, and $2 \times 2 \times 1$ Monkhorst Pack k-point sampling was chosen for the well converged energy values of $\text{FeN}_4\text{-OH}$, $\text{FeN}_3\text{-O}$, FeN_3 and FeN_4 slabs, respectively. Geometry optimizations were pursued until the force on each atom falls below the convergence criterion of 0.02 eV/\AA and energies were converged within 10^{-6} eV . Moreover, all calculations were spin polarized. More details of the DFT calculations can be found in the supporting information.

3. Results and discussion

3.1. Characterization of the $\text{Fe}_1/\text{CN-X}$ catalysts

Single-atom Fe catalysts supported on carbon-based materials ($\text{Fe}_1/\text{CN-X}$) were prepared by combining ball-milling and pyrolysis treatments (Fig. 1). The scanning electron microscopy (SEM) images of $\text{Fe}_1/$

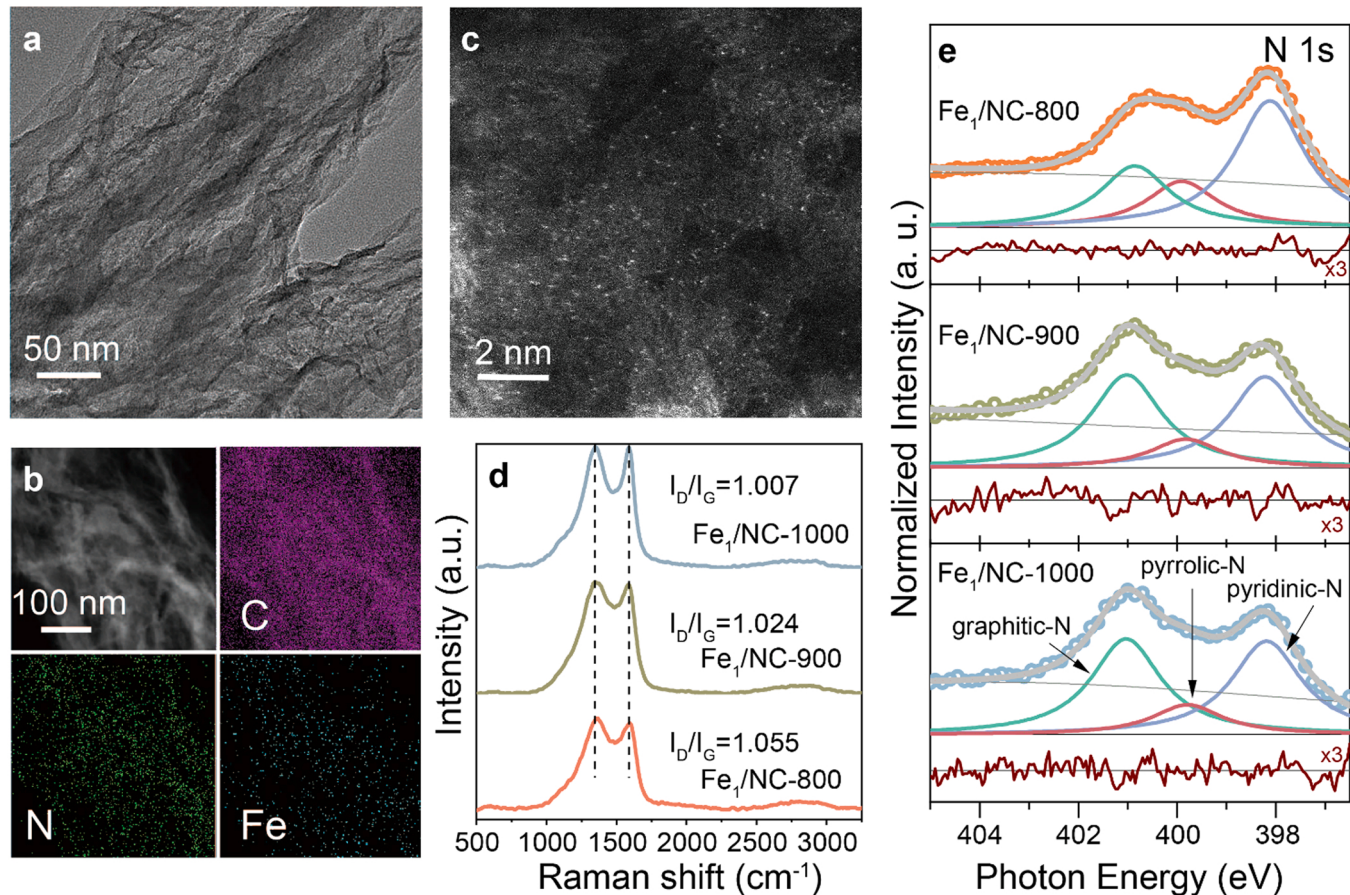


Fig. 2. (a) TEM image, (b) STEM-EDX elemental mapping images, and (c) HADDF-STEM image of the $\text{Fe}_1/\text{CN-900}$. (d) Raman spectra and (e) XPS N 1 s core-level spectra of $\text{Fe}_1/\text{NC-800}$, $\text{Fe}_1/\text{NC-900}$, and $\text{Fe}_1/\text{NC-1000}$ catalysts.

CN-800, Fe₁/CN-900, and Fe₁/CN-1000 present integrated and sheet-like CN materials (Fig. S1). More detailed structures of Fe/NC were further demonstrated by High-resolution transmission electron microscopy (TEM) images (Figs. 2a and S2), revealing ultrathin two-dimensional (2D) nanosheets over the entire carbon matrix, supporting a high surface area. The large surface area would make single Fe atoms easily accessible. Accordingly, the energy dispersive x-ray spectroscopy (EDX) elemental mapping demonstrates the isolated and homogeneously distributed Fe atoms throughout the samples (Figs. 2b and S2), reflecting atomically dispersed Fe sites. Furthermore, the high dispersion of Fe atoms on N-doped graphene is clearly confirmed by aberration-corrected high-angle annular dark field scanning transmission electron microscopy (HAADF-STEM) in the Figs. 2c and S3. The x-ray diffraction (XRD) data indicates that no diffraction of Fe-containing species is identifiable (Fig. S4), in accordance with TEM observations. The Raman spectra of Fe₁/NC-800, Fe₁/NC-900, and Fe₁/NC-1000 catalysts display similar but low intensity ratios ($I_D/I_G \approx 1.00$), illustrating their high graphitization degree (Fig. 2d). Moreover, x-ray photoelectron spectroscopy (XPS) results (Figs. 2e and S5) clearly demonstrate low Fe loading contents (<1 wt%) since the nearly indistinguishable Fe 2p signal is close to the detection limits of XPS ranging from 0.1 to 1 at% (Fig. S5, Inset). This agrees well with the inductively coupled plasma optical emission spectroscopy (ICP-OES) analysis of Fe₁/NC-X (Table S1). Meanwhile, N 1 s spectra (Fig. 2e) indicates that the concentrations of N decrease with heating temperature, i.e., both the pyridinic-like N and pyrrolic-like N decreases with the increase of graphitic N, consistent with Raman results. Above results confirm the formation of isolated Fe atoms in Fe₁/NC-X.

3.2. NO₃RR performances

NO₃RR activities were evaluated in a typical H-type electrolytic cell. Fig. 3a displays linear sweep voltammetry (LSV) curves of NO₃RR. Clearly, the Fe₁/NC catalyst show much higher current density in KNO₃/K₂SO₄ solution than that in K₂SO₄ solution, and the increased current density dominantly originates from electrocatalytic reduction of NO₃. Furthermore, Fe₁/NC-900 delivers higher current density at all test potentials with a specific current density of 44.1 mA cm⁻² at -0.99 V, much higher than Fe₁/NC-800 and Fe₁/NC-1000. The indophenol blue spectrophotometric method was used to quantify the produced ammonia (Fig. S6). With the potential decreasing from -0.4 V to -0.9 V, FE displays a volcanic trend, and NH₃ YR increases gradually (Fig. 3b and c). In comparison, the Fe₁/NC-900 outperforms other catalysts and delivers ca. 18.8 mgNH₃ h⁻¹ mg_{cat}⁻¹ at -0.9 V with a maximum FE of 86% at -0.7 V vs. RHE. The slightly deteriorated FE at more negative potentials is ascribed to the competing HER. Accordingly, the NH₃ current density of Fe₁/NC-900 is 10.97 mA cm⁻², and the turnover frequency is 651390 h⁻¹ at -0.7 V vs. RHE (Figs. S7 and S8). The main by-product of the NO₃RR is NO₂, which is detected and quantified by UV-vis spectroscopy (Figs. S9 and S10). Notably, NO₂ is detected in all potential ranges of all catalysts, and the yields of NO₂ increase with the potential. Fig. 3d shows that the YR of NH₃ increases along with the prolonging of electrolysis time, while FE does not change, remaining about 85% within 90 min, confirming the superior stability of the Fe₁/NC-900.

The durability of Fe₁/NC-900 for NO₃RR is further verified by 20 consecutive electrolysis cycles (Fig. 4a). The NH₃ YR and FE fluctuate

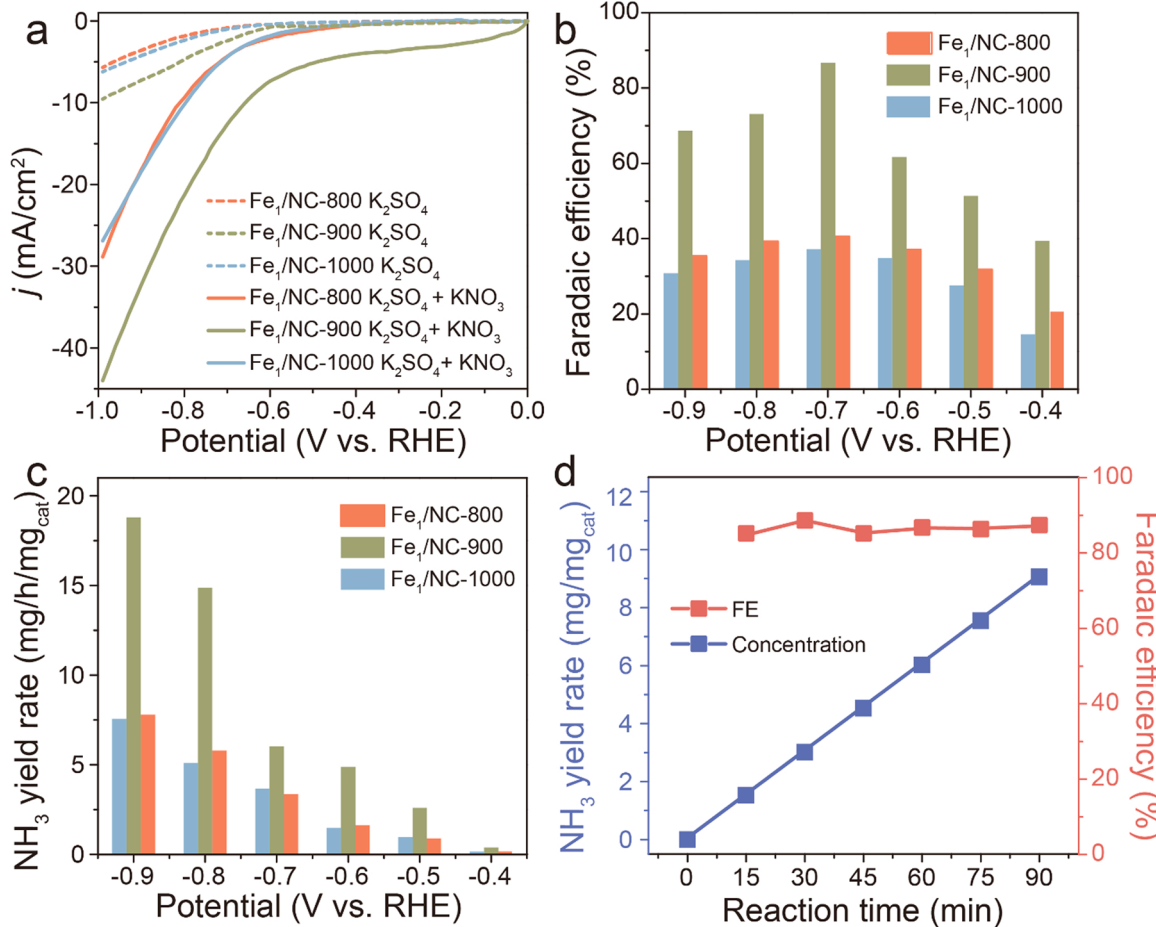


Fig. 3. (a) LSVs of the Fe₁/NC-X in 0.1 M K₂SO₄ solution with or without 0.5 M KNO₃, respectively. (b) FE of NH₃ of the Fe₁/NC-X at different potentials, (c) The corresponding NH₃ YRs of the Fe₁/NC-X at different potentials. (d) Time-dependent change of NH₃ concentration and FE over Fe₁/NC-900 at -0.7 V vs. RHE.

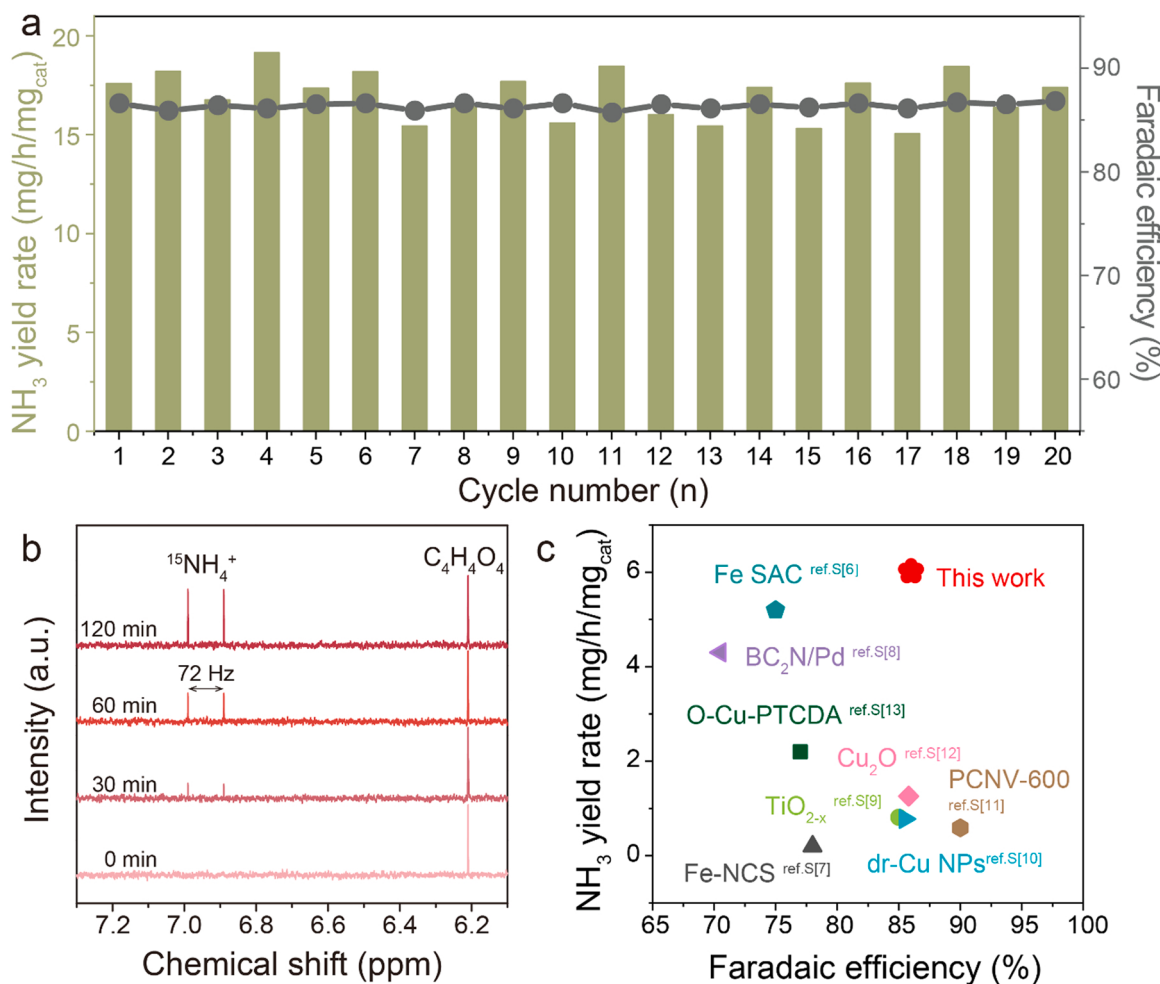


Fig. 4. (a) The cyclic stability test of Fe₁/NC-900. (b) ¹H NMR spectra of electrolytes after ¹⁵NO₃ reduction tests at different time at -0.7 V. (c) Performance comparison with other state-of-the-art NO₃RR electrocatalysts.

slightly in each cycle, indicating that the catalyst has excellent stability. Additionally, HADDF-STEM images of used Fe₁/NC-900 after recycling test show that the structure maintains unchanged (Fig. S11).

Nuclear magnetic resonance (NMR) was employed to confirm the formation of NH₃ from NO₃ ions using ¹⁵NO₃. The peak of ¹⁵NH₄⁺

displays as doublets using ¹⁵NO₃, while a triplet of ¹⁴NH₄⁺ is acquired when the nitrogen source is switched to ¹⁴NO₃ (Figs. 4b and S12). The ¹H NMR spectra of the electrolyte after reduction of K¹⁵NO₃ shows typical double peaks of ¹⁵NH₄⁺ at *d* = 6.89 and 6.99 ppm, and the peak intensity increases with the electrolysis time, confirming that NH₃ is

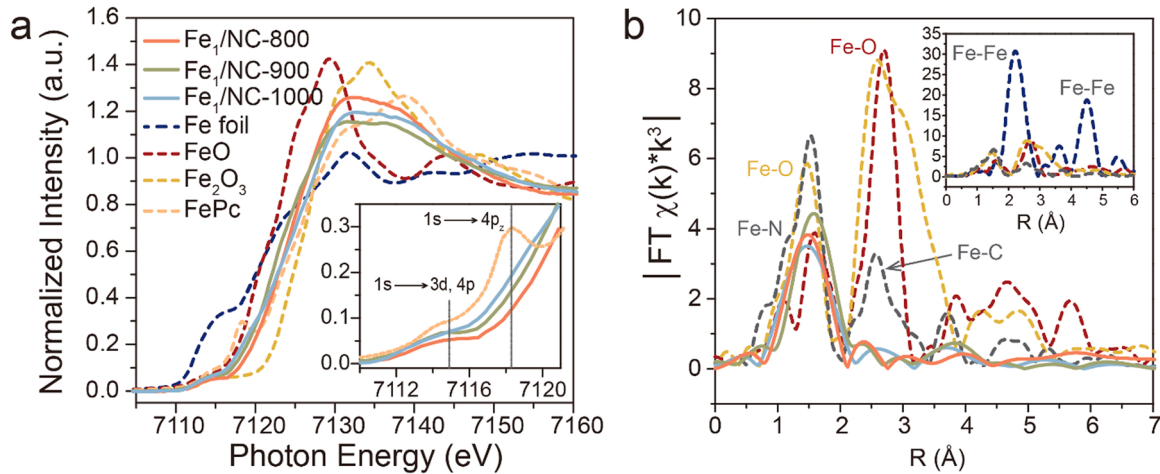


Fig. 5. (a) Normalized XANES spectra at Fe K-edge of Fe₁/NC-X along with reference materials. The inset displays an expanded view of the 1s → 3d pre-edge region, with data of FePc reference included for comparison. (b) FT-EXAFS analysis at the Fe K-edge resulting in *R*-space, showing the surrounding atoms adjacent to the Fe centers.

from NO_3RR . Additionally, no NH_3 is detected if KNO_3 is absent in the electrolyte. The produced NH_4^+ is also quantified using ^1H NMR. Upon introducing the external standard of maleic acid, the peak area of NH_4^+ displays a good linear relationship with that of maleic acid (Fig. S13). After reaction for 1 h, the yield of $^{15}\text{NH}_3$ is $6.38 \text{ mg}_{\text{NH}_3} \text{ h}^{-1} \text{ mg}_{\text{cat}}$ (Table S2), consistent with the colorimetric method, $\text{Fe}_1/\text{NC}-900$ exhibits a competitive FE and YR, outperforming other reported NO_3RR electrocatalysts (Fig. 4c and Table S3).

3.3. Identification of atomic and geometric structure of Fe-N_x

To unveil the structural nature of the Fe centers of the catalysts for NO_3RR , element-selective x-ray absorption fine structure (XAFS) spectroscopy including x-ray absorption near-edge structure (XANES) and extend x-ray absorption fine structure (EXAFS) at the Fe K-edge ($1s \rightarrow 4p$) was employed to explore the local atomic and geometric structure of the Fe active centers. The XANES spectra of these species (Fig. 5a) exhibit similar rising-edge structures (i.e., the energy position and spectral shape) to that of FePc but completely different from those of Fe foil and its oxides. Notably, the spectral weight from Fe_2O_3 was interrogated for a small but measurable Fe-O signal that should be treated with some caution. The onset of these rising-edges possesses a weak pre-edge peak (Fig. 5a, Inset), largely associated with the electric dipole-forbidden but quadrupole-allowed transitions $1s \rightarrow 3d$ (from $3d$ - $4p$ hybridized orbitals), which will be discussed later [31–34]. The EXAFS Fourier transform (FT) of the Fe K-edge (Fig. 5b) demonstrates a major peak at $1.49 \pm 0.10 \text{ \AA}$ belonging to the Fe-N(O) scattering path, while the signals at 2.2 – 2.6 \AA assigned to either Fe-Fe or Fe-C interaction are not detected. It indicates that the metals in $\text{Fe}_1/\text{NC-X}$ dominantly exist as mononuclear Fe centers without the presence of Fe-containing crystalline particles. Most likely, it would turn out to be a characteristic of the

FeN_xO_y configuration. It is noteworthy that high temperature in Ar atmosphere will result in a large amount of oxygen released. The coordination configurations for the FeN_xO_y moieties in $\text{Fe}_1/\text{NC-X}$ were then systematically examined by quantitative EXAFS curve-fitting analysis. First, the EXAFS simulation of $\text{Fe}_1/\text{NC-X}$ was analyzed assuming the presence of one or two axial oxygen ligands via two backscattering paths: Fe-N and Fe-O based on the above FT-EXAFS results (Fig. S14–16, Tables S4–6, and Note S1). During the fitting procedure, the first shell of $\text{Fe}_1/\text{NC}-800$ cannot be adequately fit with a single Fe-N scattering path (Table S5), pointing out the need to include oxygen ligand along the axial direction. Introducing an additional oxygen atom or end-on dioxygen worsens the correlation among the structural parameters for $\text{Fe}_1/\text{NC}-900$ and $\text{Fe}_1/\text{NC}-1000$ with a low reliability (Table S6). The best-fit analysis of the first-shell EXAFS data is shown in both k (Fig. S16) and R space (Fig. 6a), with extracted structural parameters listed in Table S6. The dominant contribution to the signal appearing at $1.49 \pm 0.10 \text{ \AA}$ is given by Fe-N and Fe-O first shell coordination for $\text{Fe}_1/\text{NC}-800$, whereas it is well assigned to Fe-N first shell coordination for $\text{Fe}_1/\text{NC}-900$ and $\text{Fe}_1/\text{NC}-1000$. The average coordination numbers of N and O atoms in the first coordination sphere of $\text{Fe}_1/\text{NC}-800$ are estimated to be 3.81 ± 1.15 and 0.96 ± 0.37 at distances of 2.00 ± 0.04 and $2.07 \pm 0.15 \text{ \AA}$, respectively. For $\text{Fe}_1/\text{NC}-900$ and $\text{Fe}_1/\text{NC}-1000$, the average coordination numbers of the N atoms in the first coordination sphere are estimated to be 3.14 ± 0.91 and 4.41 ± 0.60 at distances of 2.03 ± 0.03 and $2.02 \pm 0.01 \text{ \AA}$, respectively. The as-determined Fe-N distance 2.00 – 2.03 \AA agrees well with those determined for FePc by DFT predictions [35]. Very importantly, an increased Fe-O distance $2.07 \pm 0.15 \text{ \AA}$ presents for $\text{Fe}_1/\text{NC}-800$ relative to the typical Fe-O bonds $\sim 1.96 \text{ \AA}$, most likely suggesting the Fe-OH bonding along the axial direction. Considering that EXAFS results are for the average local atomic environment of Fe, it is largely impossible to determine the precise

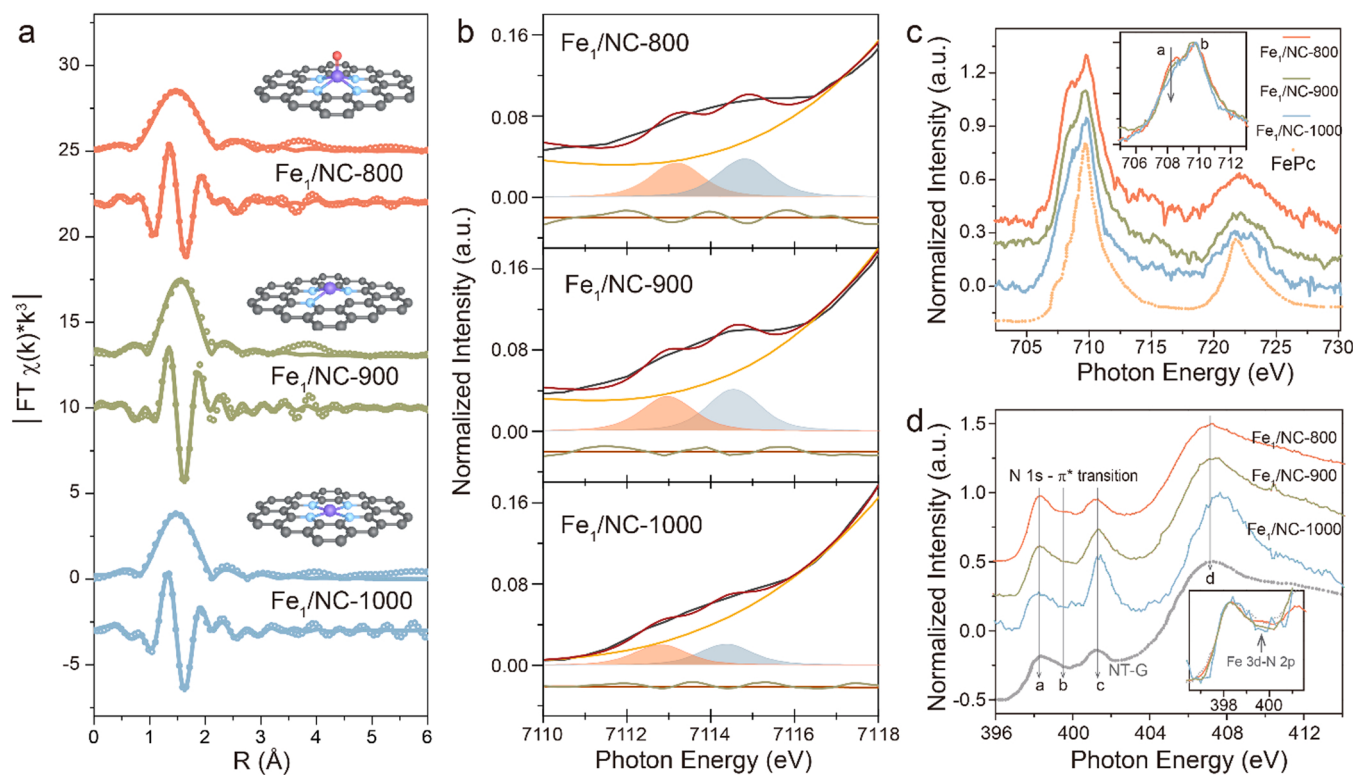


Fig. 6. (a) Fe K-edge EXAFS spectra (dots) and the corresponding curve-fits (solid lines) of $\text{Fe}_1/\text{NC-X}$, shown in R -space (including FT magnitude and imaginary component). The data are k^3 -weighted without phase correction. (b) Normalized pre-edge spectra extracted from Fe K-edge XANES of $\text{Fe}_1/\text{NC-X}$, including the experimental data (black lines), a fit to the data (red lines), the background function (yellow lines), and the residual (wine lines). (c) Fe $L_{3,2}$ -edge and (d) N K-edge XAS spectra normalized to the maximum intensity, together with that of FePc and NT-G (i.e., Fe dispersed in a nanotube-graphene complex) reference obtained from Ref. [45].

structure.

Experimental insight into valence and site geometry concerning the Fe centers can be obtained from the pre-edge ($1s \rightarrow 3d$) feature of Fe K-edge XANES spectra [34,36,37]. Contributions to pre-edge intensities with their energy positions and splitting as well as intensity distribution were determined by fitting to the data (Fig. 6b) and the parameters are present in Table 1. The pre-edge information for Fe^{2+}Pc (Fig. S17 and Note S2) and reduced Fe^{2+}Pc is also included for comparison [38]. All $\text{Fe}_1/\text{NC-X}$ spectra display split pre-edge features with a bimodal energy distribution peaking at 7113.0 ± 0.20 eV and 7114.5 ± 0.20 eV. The two main peaks exhibit a shift of +1.0 eV and +0.5 eV relative to the centroid positions of Fe^{2+} (~7112.0 eV) and Fe^{3+} (~7114.0 eV) oxide references, respectively, suggesting mostly related Fe^{3+} oxidation in $\text{Fe}_1/\text{NC-X}$ [39]. Similar values are found in the relative intensity of the two components, but the sum of the two contributions is different. The normalized pre-edge intensities for $\text{Fe}_1/\text{NC-800}$ (~0.147) and $\text{Fe}_1/\text{NC-900}$ (~0.153) are both similar to that of the FePc reference (~0.144), consistent with those characteristics of crystalline FePc (~0.115) and five-coordinate Fe^{3+} macrocycles [38,40,41]. Hence, the existence of a six-coordinated FeN_6 center (mostly considered as an octahedral geometry) in $\text{Fe}_1/\text{NC-800}$ is excluded. However, $\text{Fe}_1/\text{NC-1000}$ exhibits a pre-edge intensity (~0.081) that is a factor of approximately 2 less intense than others, closely attributed to less efficient hybridization of $3d\text{-}4p$ orbitals. More important is the appearance of an incompletely resolved pre-edge peak at ~7118.0 eV in $\text{Fe}_1/\text{NC-1000}$, which is characteristic of four-coordinate square-planar complex of Fe^{3+} [42]. It needs to distinguish itself from the one at ~7116.0 eV for reduced Fe^{2+}Pc , which is characteristic of Fe^{2+} four-coordinate square-planar geometry [43]. In addition, $\text{Fe}_1/\text{NC-1000}$ possesses a nearly equal magnitude of the pre-edge feature to reduced Fe^{2+}Pc , precluding the possibility of a FeN_3O moiety. By analogy with those changes, it is concluded that all Fe active centers in the $\text{Fe}_1/\text{NC-X}$ catalysts have a dominant Fe^{3+} character, while the variation in intensity seems to be related to the distortion of the Fe symmetry sites [39, 44]. Overall, the Fe environment in $\text{Fe}_1/\text{NC-800}$ and $\text{Fe}_1/\text{NC-900}$ is supposed to be square-based pyramidal with an axial OH ligand (OH-Fe-N_4) and a trigonal pyramidal (Fe-N_3 , most likely corresponding to tetrahedral environment with Fe at the apex) geometry, respectively. While $\text{Fe}_1/\text{NC-1000}$ exhibits a slightly broken square-planar (Fe-N_4)

geometry without axial ligand (Fig. 6a, Inset).

Following XAFS analysis, the soft-XAS was performed at Fe $L_{2,3}$ - and N K-edge to confirm the average Fe coordination environment. The Fe $L_{2,3}$ -edge (Fe $2p \rightarrow 3d$) spectra (Fig. 6c) result from electronic transitions from Fe $2p_{3/2,1/2}$ core levels (corresponding to the L_3 edge from ~706 eV to ~715 eV, and the L_2 edge from ~718 eV to ~726 eV) to unoccupied Fe 3d electronic states. The overall multiple structure of Fe L-edge spectra is very similar to that of FePc , suggesting the presence of Fe-N bonding [45–47]. In addition, the Fe L-edge signal is rather weak despite the use of the surface-sensitive TEY mode to collect the spectra. This excludes a significant Fe-enrichment on the surface. Detailed structural differences are specified by focusing on the L_3 -edge region (Fig. 6c, Inset), which is further split by the ligand field due to final state effects. The split L_3 peak becomes sharper with temperature, i.e., an increased intensity ratio of peak "b" to peak "a", as indicated by arrow. It has been most likely considered as contribution from the N $2p\text{-Fe 3d}$ transition due to Fe-N hybridization, as inferred by an enhanced orbital-overlapping between the central Fe 3d and the ligand N $2p$ -orbitals in $\text{Fe}_1/\text{NC-X}$ upon heating. Notably, for $\text{Fe}_1/\text{NC-800}$, it will be associated with the Fe 3d-N 2p, O 2p hybridization, consistent with the average Fe-N(O) bond distance determined by EXAFS simulation. The Fe-N bonding in $\text{Fe}_1/\text{NC-X}$ is further confirmed in N K-edge spectra (Fig. 6d). Similar to the NT-G reference, the N K-edge spectra mainly consists of four features: the peaks "a" (~398.3 eV) and "c" (~401.3 eV) are assigned to π^* transition to pyridinic and pyrrolic states, respectively, and the broad peak "d" (~407.6 eV) is due to C-N σ^* transitions [45,48]. It should be emphasized that the peak "b" located at ~399.5 eV (Fig. 6d, Inset) is related to the Fe-N bonding, probably corresponding to the excitations from N 1s to N 2p mixed into unoccupied Fe 3d-orbitals (i.e., Fe 3d-N 2p hybridization). Although it is difficult to elucidate quantitatively, the existence of this small peak further corroborates the formation of Fe-N coordination.

3.4. Electrolysis mechanism of NO_3RR

Based on the NO_3RR performance and the active site structure of the catalyst, we established a clear structure-performance relationship of $\text{Fe}_1/\text{NC-X}$, which provides a basis for studying the reaction pathway and mechanism of NO_3RR . *Operando* ATR-SEIRAS is a powerful tool for

Table 1

Results of a multiple peak fit to the Fe K pre-edge peak of FePc reference, reduced Fe^{2+}Pc , and $\text{Fe}_1/\text{NC-X}$ using the pseudo-Voigt functions [38].

Sample	Energy ^a (± 0.05 eV)	Intensity ^b	ΔE (± 0.07 eV)	Total intensity	Ligation ^c	Estimated geometry
FePc^d	7113.5	0.065	1.4	0.144	4 N + O	square pyramidal with an oxygen atom in the axial direction
	7114.9	0.079	–	–		
	7116.4 ^e	0.086	–	–		
	7118.0 ^f	0.289	–	–		
	7119.0 ^g	0.132	–	–		
Reduced Fe^{2+}Pc^h	7112.4	0.093	–	0.093	4 N	square-planar D_{4h}
	7116.0	–	–	–		
$\text{Fe}_1/\text{NC-800}$	7113.2	0.068	1.6	0.147	4 N + O	square pyramidal with a OH at the apex
	7114.8	0.079	–	–		
$\text{Fe}_1/\text{NC-900}$	7113.0	0.071	1.6	0.153	3 N	trigonal-pyramidal with Fe at the apex
	7114.6	0.082	–	–		
$\text{Fe}_1/\text{NC-1000}$	7112.8	0.040	1.6	0.081	4 N	slightly broken square-planar
	7114.4	0.041	–	–		
	7118.0 ^f	0.035	–	–		
	7119.7 ^g	0.039	–	–		

^a Peak energy recorded at peak maximum with uncertainty of ± 0.20 eV.

^b Intensity obtained from the integrated area with estimated uncertainty of $\pm 10\%$ were determined by fits to the data (see the Note S1, for details on the fitting procedure).

^c The ligation is obtained from the above EXAFS simulation.

^d FePc reference used here is correspond to Fe^{3+}Pc due to more easily be oxidized when exposed to oxygen.

^{e,f} The high-energy shoulders centered at around 7116.4 eV and 7118.0 eV are typically related to a $1s \rightarrow 4p_z$ shakedown transition character for square-planar Fe-N ligation of Fe^{2+} and Fe^{3+} , respectively.

^g In some cases, additional pseudo-Voigt components were necessary to mimic shoulders on the rising-edge over 7118.0 eV to obtain a good match to the data.

^h Microcrystalline Fe^{2+}Pc powder in the reduced state with four-coordinate, square-planar Fe-N ligation of Fe^{2+} , i.e., no axial ligands [38].

identifying reaction intermediates in NO_3RR (Figs. 7a and S18). When the potential is applied from 0 V to -0.9 V, the peaks of nitrogen-containing species in $\text{KNO}_3/\text{K}_2\text{SO}_4$ electrolyte vary in comparison with that in K_2SO_4 electrolyte (Fig. S19). NO_3RR can easily occur below 0 V. When the voltage further decreases, several peaks are synchronously observable, originating from different nitrogen-containing intermediates. The bands at 1250 cm^{-1} , 2162 cm^{-1} and 1355 cm^{-1} , 1410 cm^{-1} are ascribed to stretching vibration mode of $^*\text{N-O}$ and $^*\text{NO-H}_X$, respectively (Fig. 7b, c, e), confirming the deoxygenation steps during NO_3RR [49–51]. The broad band at 1643 cm^{-1} and 3436 cm^{-1} is assigned to the bending vibration mode of H_2O in the electrolyte and the O-H stretching vibration of the interface water, respectively (Fig. 7d, f). The peaks from N-H bond are also observed. The board band around 3292 cm^{-1} corresponds to $\nu(\text{N-H})$ stretching mode of NH_y species, while the bands at 1683 cm^{-1} signify the related $\sigma(\text{N-H})$ bending mode [52, 53]. These signals of NH_y species reflect the substantial hydrogenation for NH_3 evolution after deoxygenation. When using isotope-labeled K^{15}NO_3 as the $^{15}\text{NO}_3^-$ source, we observed the isotopic frequency shifts, confirming the assignment of the above nitrogen-containing species. From 0 V to -0.9 V, obvious red-shift of the bands appeared due to the decrease of $^{15}\text{NO}_3^-$.

Based on *operando* ATR-SEIRAS results, we proposed the reaction pathway of NO_3RR on $\text{Fe}_1/\text{NC}-900$ as shown in Fig. 8. After the nitrate is adsorbed on FeN_3 , ammonia is formed first through a series of deoxygenation reactions, $^*\text{NO}_3 \rightarrow ^*\text{NO}_2 \rightarrow ^*\text{NO} \rightarrow ^*\text{N}$, and then by a series of hydrogenation reactions, $^*\text{N} \rightarrow ^*\text{NH} \rightarrow ^*\text{NH}_2 \rightarrow ^*\text{NH}_3$.

To examine the effect of coordination environment of the catalysts on the NO_3RR activity, DFT study was performed to investigate the reaction mechanism of NO_3RR . Based on reaction pathway proposed by *operando* ATR-SEIRAS results, we calculated the corresponding free energy of each step of NO_3RR with the aid of DFT (Figs. 9 and S20). Firstly, NO_3^- is protonated into HNO_3 followed by chemically adsorbed

on catalyst surface. Secondly, the N-O bonds are continuously cleaved to form NO_2^* , NO^* , and N^* sequentially. Finally, N^* intermediate is stepwise hydrogenated to NH^* , NH_2^* , and NH_3^* . Specifically, the protonation of NO^* to HNO^* ($\text{NO}^* \rightarrow \text{HNO}^*$) on all catalysts is the RDS, requiring an energy barrier (ΔG) of $+0.55\text{ eV}$, $+0.26\text{ eV}$, and $+0.42\text{ eV}$, respectively. Notably, $\text{Fe}_1/\text{NC}-900$ displays the lowest ΔG ($+0.26\text{ eV}$), explaining why FeN_3 is most active among the catalysts. The free energy for HNO^* to $^*\text{N}$ ($\text{HNO}^* \rightarrow \text{N}^*$) is $+0.27\text{ eV}$ and $+0.12\text{ eV}$ on $\text{Fe}_1/\text{NC}-800$ and $\text{Fe}_1/\text{NC}-1000$, respectively, while a negative free energy is achieved on $\text{Fe}_1/\text{NC}-900$ (-0.40 eV), reflecting a spontaneous process. In addition, for $\text{Fe}_1/\text{NC}-900$, the hydrogenation step of NH_2^* to NH_3^* ($\text{NH}_2^* \rightarrow \text{NH}_3^*$) is a RDS with only $+0.18\text{ eV}$ of energy barrier. Combined with the partial density of states (PDOS) of Fe-N_3 reveals the d-band electron distribution of Fe-N_3 is closer to Fermi energy level (EF), which enhances the adsorption of NH_2^* and NH_3^* intermediates, leading to a lower energy barrier of RDS (Fig. 10b). The above results verify the impact of coordination environment on NO_3RR activity.

DOS of 3d orbitals of $\text{FeN}_4\text{-OH}$, FeN_3 , and FeN_4 coordination are derived by DFT calculations (Fig. S21). The 3d state of FeN_3 is highly localized with d_{xy} and d_{xz} -orbitals cross the E_F . Furthermore, PDOS (Fig. 10a-c) shows that the adsorbed NO_3^- exhibits a stronger overlap between Fe d-orbital and O p-orbital on FeN_3 than those on $\text{FeN}_4\text{-OH}$ and FeN_4 . The PDOS also shows obvious contributions of Fe 3d and O 2p orbital close to the E_F of FeN_3 , validating the interaction between Fe atoms and O atoms in NO_3^- . This indicates that the Fe site at the apex of the tetrahedral in the active site of FeN_3 is more favorable for nitrate adsorption. We further calculated the charge density differences of FeN_4 , FeN_3 , and $\text{FeN}_4\text{-OH}$ coordination in the $\text{Fe}_1/\text{NC-X}$ (Fig. S22). In FeN_4 and $\text{FeN}_4\text{-OH}$, electrons are accumulated near the coordination N atoms and consumed near the Fe atoms, whereas in FeN_3 , electrons are accumulated at Fe and N sites and enhanced charge transfer. Fig. 10d-f shows the charge density difference of adsorbed NO_3^- molecules on these sites.

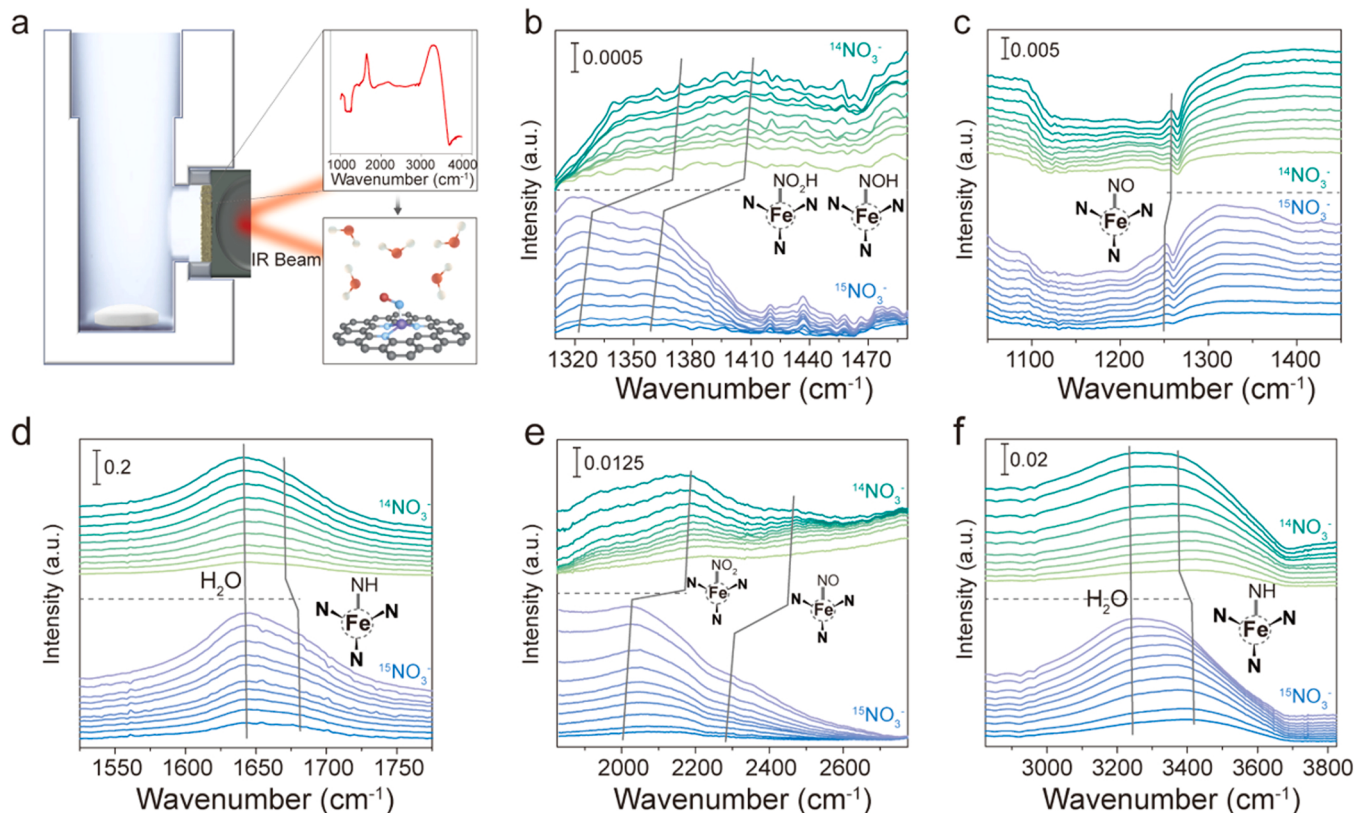


Fig. 7. (a) Schematic of the tailor-made electrolytic cell for *operando* ATR-SEIRAS characterization. (b-f) *operando* ATR-SEIRAS spectra of $\text{Fe}_1/\text{NC}-900$ in $\text{KNO}_3 + \text{K}_2\text{SO}_4$ (top) and $\text{K}^{15}\text{NO}_3 + \text{K}_2\text{SO}_4$ (bottom) electrolyte at different applied potentials.

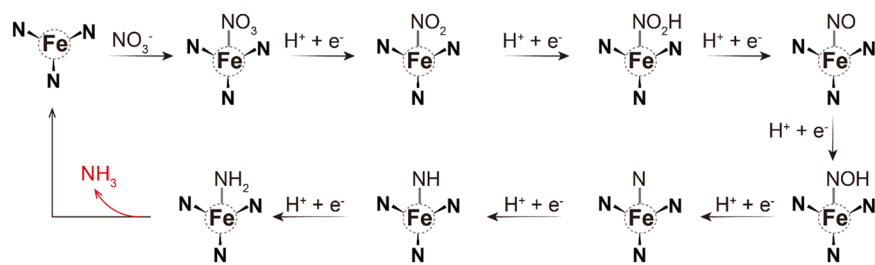


Fig. 8. Schematic illustration of electrocatalytic nitrate-to-ammonia reaction pathway on FeN_3 .

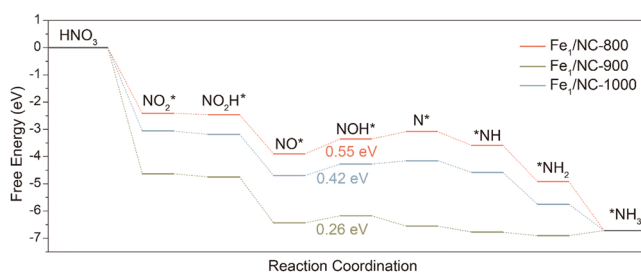


Fig. 9. Reaction free energies for different intermediates on $\text{Fe}_1/\text{NC}-800$, $\text{Fe}_1/\text{NC}-900$, and $\text{Fe}_1/\text{NC}-1000$.

When NO_3^- is adsorbed, the Fe site acts as an activation center, accelerating the migration of electrons towards NO_3^- and increasing electron density of NO_3^- . Compared with other active sites, FeN_3 has numerous lone pair electrons, favoring the formation of strong Fe-O bond between NO_3^- and Fe sites. Accordingly, the Fe-O bond lengths are shortened to 1.988 Å and 1.990 Å in Fe-N_3 , confirming the stronger adsorption of NO_3^- .

4. Conclusion

To sum up, we developed a series of $\text{Fe}_1/\text{NC-X}$ through thermal

regulation, and the local structure was systematically analyzed by XAFS and soft XAS. The results show that the main active sites of $\text{Fe}_1/\text{NC}-800$, $\text{Fe}_1/\text{NC}-900$ and $\text{Fe}_1/\text{NC}-1000$ are $\text{Fe-N}_4\text{-OH}$, Fe-N_3 and Fe-N_4 , respectively. $\text{Fe}_1/\text{NC}-900$ displays the highest NO_3RR activity with a FE of 86.7% at -0.7 V, and a YR of $18.8 \text{ mg}_{\text{NH}_3} \text{ h}^{-1} \text{ mg}_{\text{cat}}^{-1}$ at -0.9 V vs. RHE. The ^{15}N isotope labeling experiments reveal that ammonia originates from NO_3RR . *Operando* ATR-SEIRAS and DFT simulations show that $\text{Fe}_1/\text{NC}-900$ exhibits high activity in NO_3RR due to more lone pair electrons of Fe-N_3 active site, and the Fe site at the apex of the tetrahedral is more favorable for nitrate adsorption, intensifying charge transfer, and lowering the energy barrier of the RDS. This study not only proves the impact of the coordination structure on NO_3RR performance, but also offers a feasible method to identify the coordination structure of the metal active site in M-NC catalyst.

CRediT authorship contribution statement

Lingyue Liu: Conceptualization, Data curation, Formal analysis, Methodology, Investigation, Writing – original draft, Visualization. **Ting Xiao:** Conceptualization, Formal analysis, Writing – original draft. **Heyun Fu:** Supervision, Writing – review & editing. **Zhongjun Chen:** Resources. **Xiaolei Qu:** Supervision, Writing – review & editing, Funding acquisition. **Shourong Zheng:** Conceptualization, Methodology, Supervision, Writing – review & editing, Funding acquisition.

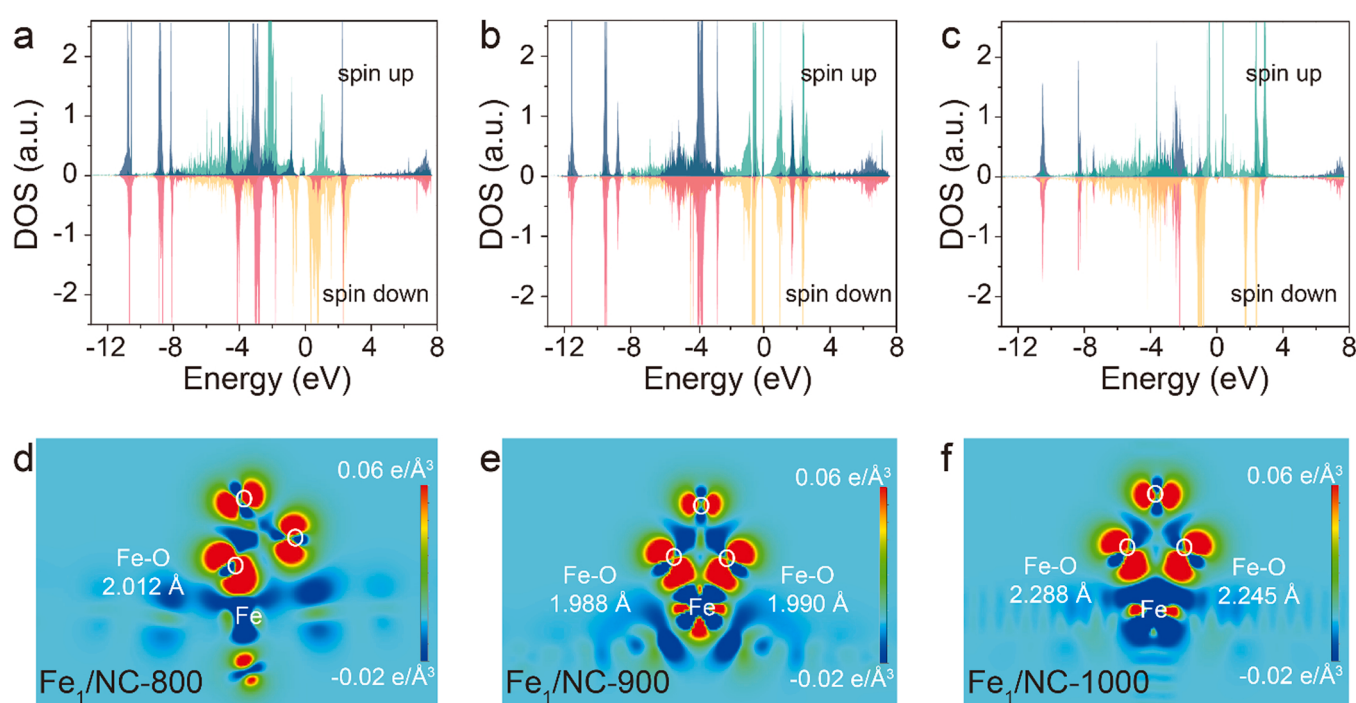


Fig. 10. PDOS of NO_3^- adsorption on (a) FeN_4 , (b) FeN_3 , and (c) $\text{FeN}_4\text{-OH}$ (green: Fe-up, yellow: Fe-down, blue: O-up, red: O-down). The differential charge density maps of NO_3^- adsorption on (d) $\text{FeN}_4\text{-OH}$, (e) FeN_3 , and (f) FeN_4 . Aquamarine to orange indicates the transition from electron depletion to accumulation.

Declaration of Competing Interest

The authors declare that they have no known competing financial interests or personal relationships that could have appeared to influence the work reported in this paper.

Data availability

Data will be made available on request.

Acknowledgments

This work was supported by the National Natural Science Foundation of China (No. 21976086) and the National Key Research and Development Program of China (No. 2019YFC1804201). The authors would like to thank facility support of the 4B9A and 4B9B beamlines of Beijing Synchrotron Radiation Facility (BSRF).

Appendix A. Supporting information

Supplementary data associated with this article can be found in the online version at [doi:10.1016/j.apcatb.2022.122181](https://doi.org/10.1016/j.apcatb.2022.122181).

References

- [1] J.G. Chen, R.M. Crooks, L.C. Seefeldt, K.L. Bren, R.M. Bullock, M.Y. Daresbourg, P.L. Holland, B. Hoffman, M.J. Janik, A.K. Jones, M.G. Kanatzidis, P. King, K. M. Lancaster, S.V. Lyman, P. Pfromm, W.F. Schneider, R.R. Schrock, Beyond fossil fuel-driven nitrogen transformations, *Science* 6391 (2018), <https://doi.org/10.1126/science.aar6611>.
- [2] G. Qing, R. Ghazfar, S.T. Jackowski, F. Habibzadeh, M.M. Ashtiani, C.P. Chen, M. R. Smith 3rd, T.W. Hamann, Recent advances and challenges of electrocatalytic N₂ reduction to ammonia, *Chem. Rev.* 120 (2020) 5437–5516, <https://doi.org/10.1021/acs.chemrev.9b00659>.
- [3] T.N. Ye, S.W. Park, Y. Lu, J. Li, M. Sasase, M. Kitano, T. Tada, H. Hosono, Vacancy-enabled N₂ activation for ammonia synthesis on an Ni-loaded catalyst, *Nature* 583 (2020) 391–395, <https://doi.org/10.1038/s41586-020-2464-9>.
- [4] W. He, J. Zhang, S. Dieckhofer, S. Varhade, A.C. Brix, A. Lielpetere, S. Seisel, J.R. C. Junqueira, W. Schuhmann, Splicing the active phases of copper/cobalt-based catalysts achieves high-rate tandem electroreduction of nitrate to ammonia, *Nat. Commun.* 13 (2022) 1129, <https://doi.org/10.1038/s41467-022-28728-4>.
- [5] H. Yin, Z. Chen, S. Xiong, J. Chen, C. Wang, R. Wang, Y. Kuwahara, J. Luo, H. Yamashita, Y. Peng, J. Li, Alloying effect-induced electron polarization drives nitrate electroreduction to ammonia, *Chem. Catal.* 1 (2021) 1088–1103, <https://doi.org/10.1016/j.jcatal.2021.08.014>.
- [6] F.Y. Chen, Z.Y. Wu, S. Gupta, D.J. Rivera, S.V. Lambeets, S. Pecaut, J.Y.T. Kim, P. Zhu, Y.Z. Finfrock, D.M. Meira, G. King, G. Gao, W. Xu, D.A. Cullen, H. Zhou, Y. Han, D.E. Perea, C.L. Muñich, H. Wang, Efficient conversion of low-concentration nitrate sources into ammonia on a Ru-dispersed Cu nanowire electrocatalyst, *Nat. Nanotechnol.* 17 (2022) 759–767, <https://doi.org/10.1038/s41565-022-01121-4>.
- [7] N.C. Kani, J.A. Gauthier, A. Prajapati, J. Edgington, I. Bordawekar, W. Shields, M. Shields, L.C. Seitz, A.R. Singh, M.R. Singh, Solar-driven electrochemical synthesis of ammonia using nitrate with 11% solar-to-fuel efficiency at ambient conditions, *Energy Environ. Sci.* 14 (2021) 6349–6359, <https://doi.org/10.1039/D1EE01879E>.
- [8] H. Xu, Y. Ma, J. Chen, W.X. Zhang, J. Yang, Electrocatalytic reduction of nitrate - a step towards a sustainable nitrogen cycle, *Chem. Soc. Rev.* 51 (2022) 2710–2758, <https://doi.org/10.1039/d1cs00857a>.
- [9] H. Niu, Z. Zhang, X. Wang, X. Wan, C. Shao, Y. Guo, Theoretical insights into the mechanism of selective nitrate-to-ammonia electroreduction on single-atom catalysts, *Adv. Funct. Mater.* 31 (2021), 2008533, <https://doi.org/10.1002/adfm.202008533>.
- [10] Y. Wang, W. Zhou, R. Jia, Y. Yu, B. Zhang, Unveiling the activity origin of a copper-based electrocatalyst for selective nitrate reduction to ammonia, *Angew. Chem. Int. Ed.* 59 (2020) 5350–5354, <https://doi.org/10.1002/anie.201915992>.
- [11] G.-F. Chen, Y. Yuan, H. Jiang, S.-Y. Ren, L.-X. Ding, L. Ma, T. Wu, J. Lu, H. Wang, Electrochemical reduction of nitrate to ammonia via direct eight-electron transfer using a copper-molecular solid catalyst, *Nat. Energy* 5 (2020) 605–613, <https://doi.org/10.1038/s41560-020-0654-1>.
- [12] S. Liu, H.B. Yang, S.F. Hung, J. Ding, W. Cai, L. Liu, J. Gao, X. Li, X. Ren, Z. Kuang, Y. Huang, T. Zhang, B. Liu, Elucidating the electrocatalytic CO₂ reduction reaction over a model single-atom nickel catalyst, *Angew. Chem. Int. Ed.* 59 (2020) 798–803, <https://doi.org/10.1002/anie.201911995>.
- [13] H.B. Yang, S.-F. Hung, S. Liu, K. Yuan, S. Miao, L. Zhang, X. Huang, H.-Y. Wang, W. Cai, R. Chen, J. Gao, X. Yang, W. Chen, Y. Huang, H.M. Chen, C.M. Li, T. Zhang, B. Liu, Atomically dispersed Ni(i) as the active site for electrochemical CO₂ reduction, *Nat. Energy* 3 (2018) 140–147, <https://doi.org/10.1038/s41560-017-0078-8>.
- [14] X. Li, Y. Zeng, C.-W. Tung, Y.-R. Lu, S. Baskaran, S.-F. Hung, S. Wang, C.-Q. Xu, J. Wang, T.-S. Chan, H.M. Chen, J. Jiang, Q. Yu, Y. Huang, J. Li, T. Zhang, B. Liu, Unveiling the in situ generation of a monovalent Fe(I) site in the single-Fe-atom catalyst for electrochemical CO₂ reduction, *ACS Catal.* 11 (2021) 7292–7301, <https://doi.org/10.1021/acscatal.1c01621>.
- [15] Y. Liu, Q. Wang, J. Zhang, J. Ding, Y. Cheng, T. Wang, J. Li, F. Hu, H.B. Yang, B. Liu, Recent advances in carbon-supported noble-metal electrocatalysts for hydrogen evolution reaction: syntheses, structures, and properties, *Adv. Energy Mater.* 12 (2022), 2200928, <https://doi.org/10.1002/aenm.202200928>.
- [16] J. Ding, J. Huang, Q. Zhang, Z. Wei, Q. He, Z. Chen, Y. Liu, X. Su, Y. Zhai, A hierarchical monolithic cobalt-single-atom electrode for efficient hydrogen peroxide production in acid, *Catal. Sci. Technol.* 12 (2022) 2416–2419, <https://doi.org/10.1039/dcyc00427e>.
- [17] J. Yang, H. Qi, A. Li, X. Liu, X. Yang, S. Zhang, Q. Zhao, Q. Jiang, Y. Su, L. Zhang, J. F. Li, Z.Q. Tian, W. Liu, A. Wang, T. Zhang, Potential-driven restructuring of Cu single atoms to nanoparticles for boosting the electrochemical reduction of nitrate to ammonia, *J. Am. Chem. Soc.* 144 (2022) 12062–12071, <https://doi.org/10.1021/jacs.2c02262>.
- [18] J. Li, M. Li, N. An, S. Zhang, Q. Song, Y. Yang, J. Li, X. Liu, Boosted ammonium production by single cobalt atom catalysts with high faradic efficiencies, e2123450119, *Proc. Natl. Acad. Sci. U. S. A.* 119 (2022), <https://doi.org/10.1073/pnas.2123450119>.
- [19] J. Li, M. Li, N. An, S. Zhang, Q. Song, Y. Yang, X. Liu, Atomically dispersed Fe atoms anchored on S and N-codoped carbon for efficient electrochemical denitrification, e2105628118, *Proc. Natl. Acad. Sci. U. S. A.* 118 (2021), <https://doi.org/10.1073/pnas.2105628118>.
- [20] P. Li, Z. Jin, Z. Fang, G. Yu, A single-site iron catalyst with preoccupied active centers that achieves selective ammonia electrosynthesis from nitrate, *Energy Environ. Sci.* 14 (2021) 3522–3531, <https://doi.org/10.1039/D1EE00545F>.
- [21] W.-D. Zhang, H. Dong, L. Zhou, H. Xu, H.-R. Wang, X. Yan, Y. Jiang, J. Zhang, Z.-G. Gu, Fe single-atom catalysts with pre-organized coordination structure for efficient electrochemical nitrate reduction to ammonia, *Appl. Catal. B* 317 (2022), <https://doi.org/10.1016/j.apcatb.2022.121750>.
- [22] Z.Y. Wu, M. Karamad, X. Yong, Q. Huang, D.A. Cullen, P. Zhu, C. Xia, Q. Xiao, M. Shakouri, F.Y. Chen, J.Y.T. Kim, Y. Xia, K. Heck, Y. Hu, M.S. Wong, Q. Li, I. Gates, S. Siahrostami, H. Wang, Electrochemical ammonia synthesis via nitrate reduction on Fe single atom catalyst, *Nat. Commun.* 12 (2021) 2870, <https://doi.org/10.1038/s41467-021-23115-x>.
- [23] R. Li, D. Wang, Understanding the structure-performance relationship of active sites at atomic scale, *Nano Res.* 15 (2022) 6888–6923, <https://doi.org/10.1007/s12274-022-4371-x>.
- [24] Y. Wang, X. Zheng, D. Wang, Design concept for electrocatalysts, *Nano Res.* 15 (2021) 1730–1752, <https://doi.org/10.1007/s12274-021-3794-0>.
- [25] X. Li, C.-S. Cao, S.-F. Hung, Y.-R. Lu, W. Cai, A.I. Rykov, S. Miao, S. Xi, H. Yang, Z. Hu, J. Wang, J. Zhao, E.E. Alp, W. Xu, T.-S. Chan, H. Chen, Q. Xiong, H. Xiao, Y. Huang, J. Li, T. Zhang, B. Liu, Identification of the electronic and structural dynamics of catalytic centers in single-Fe-atom material, *Chem* 6 (2020) 3440–3454, <https://doi.org/10.1016/j.chempr.2020.10.027>.
- [26] Y. Pan, Y. Chen, K. Wu, Z. Chen, S. Liu, X. Cao, W.C. Cheong, T. Meng, J. Luo, L. Zheng, C. Liu, D. Wang, Q. Peng, J. Li, C. Chen, Regulating the coordination structure of single-atom Fe-N_xCy catalytic sites for benzene oxidation, *Nat. Commun.* 10 (2019) 4290, <https://doi.org/10.1038/s41467-019-12362-8>.
- [27] Z. Chen, H. Niu, J. Ding, H. Liu, P.H. Chen, Y.H. Lu, Y.R. Lu, W. Zuo, L. Han, Y. Guo, S.F. Hung, Y. Zhai, Unraveling the origin of sulfur-doped Fe-N-C single-atom catalyst for enhanced oxygen reduction activity: effect of iron spin-state tuning, *Angew. Chem. Int. Ed.* 60 (2021) 25404–25410, <https://doi.org/10.1002/anie.202110243>.
- [28] J. Yang, W. Liu, M. Xu, X. Liu, H. Qi, L. Zhang, X. Yang, S. Niu, D. Zhou, Y. Liu, Y. Su, J.F. Li, Z.Q. Tian, W. Zhou, A. Wang, T. Zhang, Dynamic behavior of single-atom catalysts in electrocatalysis: identification of Cu-N₃ as an active site for the oxygen reduction reaction, *J. Am. Chem. Soc.* 143 (2021) 14530–14539, <https://doi.org/10.1021/jacs.1c03788>.
- [29] L. Cao, Q. Luo, W. Liu, Y. Lin, X. Liu, Y. Cao, W. Zhang, Y. Wu, J. Yang, T. Yao, S. Wei, Identification of single-atom active sites in carbon-based cobalt catalysts during electrocatalytic hydrogen evolution, *Nat. Catal.* 2 (2019) 134–141, <https://doi.org/10.1038/s41929-018-0203-5>.
- [30] M. Bajdich, M. Garcia-Mota, A. Vojvodic, J.K. Norskov, A.T. Bell, Theoretical investigation of the activity of cobalt oxides for the electrochemical oxidation of water, *J. Am. Chem. Soc.* 135 (2013) 13521–13530, <https://doi.org/10.1021/ja405997s>.
- [31] L.-S. Kau, D.J. Spira-Solomon, J.E. Penner-Hahn, K.O. Hodgson, E.I. Solomon, X-ray absorption edge determination of the oxidation state and coordination number of copper: application to the type 3 site in rhus vernicifera laccase and its reaction with oxygen, *J. Am. Chem. Soc.* 109 (1987) 6433–6442, <https://doi.org/10.1021/ja00255a032>.
- [32] A.L. Roe, D.J. Schneider, R.J. Mayer, J.W. Pyrz, J. Widom, J.L. Que, X-ray absorption spectroscopy of iron-tyrosinate proteins, *J. Am. Chem. Soc.* 106 (1984) 1676–1681, <https://doi.org/10.1021/ja00318a021>.
- [33] G. Dräger, R. Frahm, G. Materlik, O. Brümmer, On the multipole character of the X-ray transitions in the pre-edge structure of Fe K absorption spectra. an experimental study, *Phys. Stat. Sol. (b)* 146 (1988) 287–294, <https://doi.org/10.1002/pssb.2221460130>.

- [34] T.E. Westre, P. Kennepohl, J.G. DeWitt, B. Hedman, K.O. Hodgson, E.I. Solomon, A multiplet analysis of Fe K-edge 1s → 3d pre-edge features of iron complexes, *J. Am. Chem. Soc.* 119 (1997) 6297–6314, <https://doi.org/10.1021/ja964352a>.
- [35] C. Meneghini, L. Leboffe, M. Bionducci, G. Fanali, M. Meli, G. Colombo, M. Fasano, P. Ascenzi, S. Mobilio, The five-to-six-coordination transition of ferric human serum heme-albumin is allosterically-modulated by ibuprofen and warfarin: a combined XAS and MD study, e104231, *PLoS One* 9 (2014), <https://doi.org/10.1371/journal.pone.0104231>.
- [36] G.R. Shulman, Y. Yafet, P. Eisenberger, W.E. Blumberg, Observations and interpretation of X-ray absorption edges in iron compounds and proteins, *Proc. Natl. Acad. Sci. U. S. A* 73 (1976) 1384–1388, <https://doi.org/10.1073/pnas.73.5.1384>.
- [37] R. Sarangi, N. Aboeella, K. Fujisawa, W.B. Tolman, B. Hedman, K.O. Hodgson, E. I. Solomon, X-ray absorption edge spectroscopy and computational studies on LCuO_2 species: superoxide– Cu^{II} versus peroxide– Cu^{III} bonding, *J. Am. Chem. Soc.* 128 (2006) 8286–8296, <https://doi.org/10.1021/ja0615223>.
- [38] S. Kim, I.T. Bae, M. Sandifer, P.N. Ross, R. Carr, J. Woicik, M.R. Antonio, D. A. Scherson, In situ XANES of an iron porphyrin irreversibly adsorbed on an electrode surface, *J. Am. Chem. Soc.* 113 (1991) 9063–9066, <https://doi.org/10.1021/ja00024a006>.
- [39] L. Galoisy, G. Calas, M.A. Arrio, High-resolution XANES spectra of iron in minerals and glasses: structural information from the pre-edge region, *Chem. Geol.* 174 (2001) 307–319, [https://doi.org/10.1016/S0009-2541\(00\)00322-3](https://doi.org/10.1016/S0009-2541(00)00322-3).
- [40] M.S. Co, X-ray absorption spectroscopy of hemocyanin and hemerythrin, Stanford Univ., CA, USA, 1983.
- [41] S.M. Kauzlarich, B.K. Teo, T. Zirino, S. Burman, J.C. Davis, B.A. Averill, X-ray absorption studies of the purple acid phosphatase from beef spleen, *Inorg. Chem.* 25 (1986) 2781–2785, <https://doi.org/10.1021/ic00236a025>.
- [42] S.-Y. Ha, J. Park, T. Ohta, G. Kwag, S. Kima, *In situ* iron K-edge XANES study of iron phthalocyanine irreversibly adsorbed on an electrode surface, *Electrochim. Solid-State Lett.* 2 (1999) 461–464, <https://doi.org/10.1149/1.1390871>.
- [43] J.E. Penner-Hahn, T.J. McMurry, M. Renner, L. Latos-Grazynsky, K.S. Eble, I. M. Davis, A.L. Balch, J.T. Groves, J.H. Dawson, K.O. Hodgson, X-ray absorption spectroscopic studies of high valent iron porphyrins. horseradish peroxidase compounds I and II and synthetic models, *J. Biol. Chem.* 258 (1983) 12761–12764, [https://doi.org/10.1016/s0021-9258\(17\)44029-4](https://doi.org/10.1016/s0021-9258(17)44029-4).
- [44] T. Yamamoto, Assignment of pre-edge peaks in K-edge X-ray absorption spectra of 3d transition metal compounds: electric dipole or quadrupole, *X-Ray Spectrom.* 37 (2008) 572–584, <https://doi.org/10.1002/xrs.1103>.
- [45] J. Zhou, P.N. Duchesne, Y. Hu, J. Wang, P. Zhang, Y. Li, T. Regier, H. Dai, Fe-N bonding in a carbon nanotube-graphene complex for oxygen reduction: an XAS study, *Phys. Chem. Chem. Phys.* 16 (2014) 15787–15791, <https://doi.org/10.1039/c4cp01455c>.
- [46] P.L. Cook, X. Liu, W. Yang, F.J. Himpsel, X-ray absorption spectroscopy of biomimetic dye molecules for solar cells, *J. Chem. Phys.* 131 (2009), 194701, <https://doi.org/10.1063/1.3257621>.
- [47] P.S. Miedema, M.M. van Schoonveld, R. Bogerd, T.C.R. Rocha, M. Hävecker, A. Knop-Gericke, F.M.F. de Groot, Oxygen binding to cobalt and iron phthalocyanines as determined from *in situ* X-ray absorption spectroscopy, *J. Phys. Chem. C.* 115 (2011) 25422–25428, <https://doi.org/10.1021/jp209295f>.
- [48] J. Wang, J. Zhou, Y. Hu, T. Regier, Chemical interaction and imaging of single Co_3O_4 /graphene sheets studied by scanning transmission X-ray microscopy and X-ray absorption spectroscopy, *Energy Environ. Sci.* 6 (2013) 926–934, <https://doi.org/10.1039/c2ee23844f>.
- [49] E. Pérez-Gallent, M.C. Figueiredo, I. Katsounaros, M.T.M. Koper, Electrocatalytic reduction of nitrate on copper single crystals in acidic and alkaline solutions, *Electrochim. Acta* 227 (2017) 77–84, <https://doi.org/10.1016/j.electacta.2016.12.147>.
- [50] F.R. Rima, K. Nakata, K. Shimazu, O. Masatoshi, Surface-enhanced infrared absorption spectroscopic studies of adsorbed nitrate, nitric oxide, and related compounds. 3. formation and reduction of adsorbed nitrate at a platinum electrode, *J. Phys. Chem. C.* 114 (2010) 6011–6018, <https://doi.org/10.1021/jp911027q>.
- [51] Z. Gong, W. Zhong, Z. He, Q. Liu, H. Chen, D. Zhou, N. Zhang, X. Kang, Y. Chen, Regulating surface oxygen species on copper (I) oxides via plasma treatment for effective reduction of nitrate to ammonia, *Appl. Catal. B* 305 (2022), 121021, <https://doi.org/10.1016/j.apcatb.2021.121021>.
- [52] N. Zhang, J. Shang, X. Deng, L. Cai, R. Long, Y. Xiong, Y. Chai, Governing interlayer strain in bismuth nanocrystals for efficient ammonia electrosynthesis from nitrate reduction, *ACS Nano* 16 (2022) 4795–4804, <https://doi.org/10.1021/acsnano.2c00101>.
- [53] C. Lv, L. Zhong, H. Liu, Z. Fang, C. Yan, M. Chen, Y. Kong, C. Lee, D. Liu, S. Li, J. Liu, L. Song, G. Chen, Q. Yan, G. Yu, Selective electrocatalytic synthesis of urea with nitrate and carbon dioxide, *Nat. Sustain.* 4 (2021) 868–876, <https://doi.org/10.1038/s41893-021-00741-3>.